

Contents lists available at ScienceDirect

# Journal of the Mechanics and Physics of Solids

journal homepage: www.elsevier.com/locate/jmps



# Nonlinear optimization for compact representation of orientation distributions based on generalized spherical harmonics



Russell E. Marki, Marko Knezevic\*

Department of Mechanical Engineering, University of New Hampshire, 33 Academic Way, Kingsbury Hall, W119, Durham, NH 03824, USA

#### ARTICLE INFO

Keywords:
Orientation distribution function
Generalized spherical harmonics
Nonlinear optimization
Crystal plasticity

#### ABSTRACT

An orientation distribution is a necessary input in any crystal plasticity simulation. The computational time involved in crystal plasticity simulations scales linearly with the number of crystal orientations in the input distributions. Reducing the number of crystal orientations in representing the input orientation distributions quantitatively is a critical and necessary requirement for performing computationally efficient crystal plasticity simulations of deformation processes. A procedure for the compaction of orientation distribution functions (ODFs) relying on a spectral representation using series of generalized spherical harmonics (GSH) basis functions was recently developed. Linear fitting of the spectral representation of an ODF containing a compact set of weighted orientations towards a full-size ODF containing many crystal orientations was in the core of the procedure. This paper advances the compaction procedure by replacing the linear with a nonlinear optimization in Matlab for which a suitably defined error, gradient, and Hessian matrix are derived to allow for more efficient, accurate, and greater compactions. The utility of the new procedure is to allow for not only fitting the weights of a compacted set of orientations but to allow for optimizing weighted orientations or a combination of optimizing weights and orientations. The new compaction procedure has been successfully applied to compactions of large ODFs of cubic, hexagonal, and orthorhombic polycrystalline metals. In doing so, the evolution of texture, twinning, and stress-strain are predicted at large plastic strains with compact ODFs to agree with the corresponding full size ODFs using crystal plasticity models. In closing, guidance for effective texture compaction trading off the accuracy and computational gains are provided.

# 1. Introduction

Orientation distribution functions (ODFs) are used to quantitatively describe crystallographic texture in polycrystalline metals (Bunge, 1993). Such distributions are the normalized probability densities describing the occurrence of a given crystal orientation in the metal. Modeling the anisotropy of material properties and the evolution of such propertied during thermo-mechanical processing requires the consideration of a crystal structure and ODFs (Kocks et al., 1998). A given crystal structure and an ODF determine elastic-plastic properties and the activation of the deformation mechanisms like glide, twinning, and strain induced transformations during processing (Feng et al., 2021; Proust et al., 2007; Taylor, 1938). Material models aimed at predicting mechanical properties and texture evolution must consider the crystal structure and ODF as inputs. Reducing the number of crystal orientations per ODF is a

E-mail address: marko.knezevic@unh.edu (M. Knezevic).

<sup>\*</sup> Corresponding author.

critical and necessary step towards performing computationally efficient modeling of material properties and processes since the computational time involved in such simulations scales linearly with the number of crystal orientations. The scaling is because crystal plasticity equations for stress must be solved for every crystal orientation in every trial increment. Moreover, the memory requirements in simulations are greater for bigger ODFs. The present paper is concerned with developing a methodology for compact representation of ODFs.

Modeling of mechanical properties and processes such as deformation, recrystallization, and phase transformations can be accomplished using crystal plasticity models (Beyerlein and Tóth, 2009; Riyad and Knezevic, 2023; Rollett, 1997). The kinematics/kinetics of these deformation mechanisms in the models is physically based. The added benefit of the consideration of ODF makes these models vital in understanding and predicting the microstructure-property relationships and concomitant evolution of the microstructure. Such models have been developed based on discrete ODF inputs and their evolution. Standalone formulations of these models range from mean-field such as Taylor (Knezevic et al., 2008a; Taylor, 1938), elasto-plastic self consistent (EPSC) (Turner and Tomé, 1994; Zecevic and Knezevic, 2015; Zecevic et al., 2016c, 2019b), and visco-plastic self-consistent (VPSC) (Lebensohn and Tomé, 1993; Lebensohn et al., 2016; Zecevic et al., 2018, 2019a) to the full-field formulations such as elasto-viscoplastic fast Fourier transforms (EVPFFT) (Eghtesad et al., 2017; Lebensohn et al., 2012, 2011). These models have been coupled with finite element (FE) frameworks to become Taylor-crystal plasticity finite element (T-CPFE) (Ardeljan et al., 2014, 2016, 2015; Ardeljan and Knezevic, 2018; Feather et al., 2019, 2021; Kalidindi et al., 1992; Knezevic et al., 2014), FE-VPSC (Knezevic et al., 2013; Segurado et al., 2012; Zecevic et al., 2016a, 2016b, 2015), FE-EPSC (Zecevic et al., 2017; Zecevic and Knezevic, 2017, 2019), and FE-EVPFFT (Eghtesad et al., 2016a, 2016b, 2016b, 2016b, 2016b), FE-EPSC (Zecevic et al., 2017; Zecevic and Knezevic, 2017, 2019), and FE-EVPFFT (Eghtesad et al., 2016b). 2022) models. The embedded crystal plasticity models as constructive laws within FE frameworks facilitate anisotropic modeling of structural components and metal forming processes (Balasubramanian, 1996; Barrett and Knezevic, 2019; Barrett et al., 2018; Beaudoin et al., 1994, 1993; Knezevic et al., 2016; Raabe and Roters, 2004; Savage et al., 2018). While these works demonstrated the benefits and utility of such modeling approaches, the works also showed that such simulations are a huge computational challenge. The crystal plasticity formulations coupled with FE frameworks are computationally very demanding because texture is a state variable at each FE integration point. Clearly, speedups are needed to make such simulation approaches practical and enable their wider use (Barton et al., 2011; Panchal et al., 2013; Savage et al., 2017).

To achieve the speedups, efficient numerical implementations of crystal plasticity are being explored. Databases of precomputed solutions to basic equations of crystal plasticity are often used as an approach to circumvent solving sets of numerically stiff equations requiring a large number of iterations for every crystal orientation at every trial strain increment. One such approach involves an adaptive sampling algorithm to build a database of solutions that constantly updates itself during simulations (Barton et al., 2011, 2008). The method was able to improve efficiency by about an order of magnitude. Similarly, several approached exist in literature where precompiled solutions are in the form of spectral coefficients of continuous generalized spherical harmonics (GSH) basis (Kalidindi et al., 2006; Knezevic et al., 2008b; Shaffer et al., 2010; Wu et al., 2007) or FFTs (Al-Harbi et al., 2010; Knezevic et al., 2009; Landry and Knezevic, 2015; Zecevic et al., 2015). These implementations improve efficiency by about two orders of magnitude. A process plane concept involving the proper orthogonal decomposition in Rodrigues crystal orientation space was developed and found to yield some improvements in efficiency (Sundararaghavan and Zabaras, 2007). The Jacobian-Free Newton–Krylov (JFNK) solution procedure to crystal plasticity equations in place of Newton's method can also yield some computational benefits (Chockalingam et al., 2013).

To achieve the speedups furthermore, parallel computing implementations on specialized computer hardware are being developed. To this end, several high-performance codes as the crystal plasticity solvers have been developed to run on graphic processing units (GPUs) (Eghtesad et al., 2022; Knezevic and Savage, 2014; Mihaila et al., 2014; Savage and Knezevic, 2015).

The approaches to accelerating crystal plasticity codes could be greatly complemented by minimizing the amount of state variables, particularly those data related to ODFs. Since crystal plasticity calculations and the number of state variables involved in such calculations scale nearly linearly with the number of crystal orientations, the computational speed can substantially be reduced by the development of ODF data compaction procedures. To this end, several works approximating a given ODF with a reduced number of crystal orientations representing the given ODF exist in literature (Baudin et al., 1995; Baudin and Penelle, 1993; Pospiech et al., 1994; Wright and Adams, 1990). The works considered a suitably defined error to measure the difference between a given/measured ODF and a reduced ODF. The number of discrete orientations, which were equally weighted, was increased until the error was within acceptable tolerances. However, any ODF can be represented by a weighted set of orientations but selecting a minimal set of the discrete orientations for weighting is not a trivial task.

The use of GSH to represent ODF was introduced long time ago by Bunge (1993, 1965), Gelfand et al. (1963), Roe (1965). More recent works showed that large ODFs can be effectively compacted to a small set weighted orientations using the GSH functions (Eghtesad et al., 2018). Linear fitting of the spectral representation of an ODF containing a compact set of weighted orientations towards a full-size ODF containing many crystal orientations was in the core procedure. The linear programming problem was set to match the expansion coefficients of a compact ODF with those of the given ODF taking advantage of the linearity in the Fourier space by varying the weights of crystal orientation in the compact ODF. The success of the procedure was driven by choosing a set of crystal orientations for weighting. One method was based on binning of a given fundamental zone in the Bunge-Euler orientation space for selected crystal and sample symmetries. Another method was relying on MTEX to randomly select a set of orientations for weighting. While the first method always provided a solution, the second method iterated until arriving to the solution. While successful in compacting ODFs, the explored methods were not able to always converge and reach desired accuracy, especially for low symmetry metals.

This paper advances the GSH compaction procedure by replacing the linear with a nonlinear optimization in Matlab for which suitably defined gradient and Hessian matrix are derived. The new procedure does not only fit the weights of a compacted set of

orientations but also optimizes orientations or a combination of weights and orientations. Greater compactions to a minimum or nearly minimum can be achieved using the new procedure. The procedure has been successfully applied to compactions of large ODFs of cubic, hexagonal, and orthorhombic polycrystalline metals. In doing so, the evolution of texture, twinning, and stress-strain are predicted at large plastic strains with compact ODFs to agree with the corresponding large ODFs using a crystal plasticity model. The procedure, the case studies verifying the procedure, and several insights are described and discussed in this paper.

The remainder of the paper is organized as follows: The spectral representation of ODFs using GSH basis is described in detail in Section 2.1. The procedure for the compact reconstruction of ODFs is covered in Section 2.2. The results from several case studies involving cubic, hexagonal, and orthorhombic structures are presented in Section 3. Discussion emphasizing the tradeoffs in accuracy and computational gains is given in Section 4. Finally, conclusions are drawn in Section 5.

# 2. Methodology

This section describes the spectral representation of ODFs using GSH basis and then the procedure for the compact reconstruction of ODFs.

# 2.1. ODF and its GSH representation

ODF, f(g), is a normalized probability density function that describes the occurrence of a crystallographic orientation, g, in a sample/specimen of a material. The function is continuous, meaning that it will describe the probability for an orientation to be found in each texture. The function basically quantifies how crystal orientations are distributed in a polycrystal and is expressed as

$$f(g)dg = \frac{dV}{V}, \int_{\partial S} f(g)dg = 1,$$
(1)

where *V* is the volume of a material sample and dV is the volume increment associated with a crystal lattice orientation dg. One way to define a crystal lattice orientation is using a set of Bunge-Euler angles (Bunge, 1993). The angles transform the crystal lattice frame to the sample reference through an ordered set of three rotation angles. Therefore, each orientation is described by a set of ZXZ Bunge-Euler angles ( $\varphi_1$ ,  $\Phi$ ,  $\varphi_2$ ). Any crystal orientation must belong to the Bunge-Euler orientation space (OS) (Bunge, 1993).

GSH basis are a way of representing a continuous ODF using a set of discrete numbers. An ODF is represented using a series of GSH using (Bunge, 1993; Gelfand et al., 1963)

$$f(g) = \sum_{l=0}^{\infty} \sum_{m=-l}^{l} \sum_{n=-l}^{l} C_l^{mn} T_l^{mn}(g), \tag{2}$$

where  $C_l^{mn}$  are complex coefficients representing the ODF and  $T_l^{mn}$  is the GSH function providing a way of sampling the ODF at a discrete orientation. The index l enumerates the number of dimensions involved in the GSH series, while L will be used to denote the upper limit for the l values.  $T_l^{mn}$  is calculated as

$$T_{l}^{mn} = e^{im\varphi_2} P_{l}^{mn} (\cos\Phi) e^{in\varphi_1}, \tag{3}$$

which expands to

$$T_i^{mn} = P_i^{mn}(\cos\Phi)[(\cos m\varphi_2 \cos n\varphi_1 - \sin m\varphi_2 \sin n\varphi_1) + i(\cos m\varphi_2 \sin n\varphi_1 + \sin m\varphi_2 \cos n\varphi_1)]. \tag{4}$$

 $P_1^{mn}$  functions are (Bunge, 1993)

$$P_l^{mn}(x) = \frac{(-1)^{l-m}(i)^{n-m}}{2^l(l-m)!} \sqrt{\frac{(l-m)!(l+n)!}{(l+m)!(l-n)!}} (1-x)^{\frac{n-m}{2}} (1+x)^{\frac{n+m}{2}} \frac{d^{l-n}}{dx^{l-n}} \left[ (1-x)^{l-m} (1+x)^{l+m} \right], \tag{5}$$

and conveniently converted into the real functions using  $Q_l^{mn}(x) = i^{m+n}P_l^{mn}(x)$ . These  $Q_l^{mn}(x)$  functions are then used to calculate  $P_l^{mn}(x)$  by way of Fourier expansion with  $a_l^{mns} = Q_l^{ms}Q_l^{sn}$ , which are then used for m+n even  $P_l^{mn}(\cos\Phi) = a_l^{mn0} + 2\sum_{s=1}^l a_l^{mns}\cos\Phi$  and for m+n odd  $P_l^{mn}(\cos\Phi) = 2i\sum_{s=1}^l a_l^{mns}\sin\Phi$ . Evidently, the equations are entirely dependent on  $(\varphi_1, \Phi, \varphi_2)$  and the constant library  $a_l^{mns}$ , which has been recalculated in the present work for an increased precision of 16 digits and for L up to 64 compared to an available library from earlier works.

While two successive rotations, g and g', can be readily multiplied, the corresponding  $T_l^{mn}$  function follows from the addition theorem as (Bunge, 1993)

$$T_{l}^{mn}(g \cdot g') = \sum_{s=-l}^{s=l} T_{l}^{ms}(g) T_{l}^{sn}(g').$$
 (6)

The presence of symmetries requires  $f(g \cdot \dot{g}) = f(g)$  and  $f(\ddot{g} \cdot g) = f(g)$  in which  $\dot{g}$  is the right-handed statistical sample symmetry

operation and  $\ddot{g}$  is the left-handed physical crystal symmetry operation. These conditions are satisfied by remapping m and n into  $\mu$  and  $\nu$  and adding up all the rotated  $T_1^{mn}$  using  $\ddot{A}_i^{m\mu}$  and  $\ddot{A}_i^{n\nu}$  symmetry coefficients (Bunge, 1993)

$$\ddot{T}_{l}^{\mu\nu} = \sum_{l(n)} \sum_{l(n)} \ddot{A}_{l}^{m\mu} \dot{A}_{l}^{n\nu} T_{l}^{mn}.$$
 (7)

The symmetrized functions  $\dot{T}_l^{\mu\nu}$  having both right-handed and left-handed symmetries are used the same way as  $T_l^{mn}$  in representing an ODF,  $f(g) = \sum_{l=0}^L \sum_{\mu=1}^{M(l)} \sum_{\nu=1}^{N(l)} C_l^{\mu\nu} \dot{T}_l^{\mu\nu}$ . The limits determining the number of dimensions used for the representation, M(l) and N(l), depend on selected crystal and sample symmetries (Bunge, 1993). Note that triclinic means no symmetry so no dots on top of the functions. Taking into account a crystal (physical) symmetry at the very least and then even a sample (statistical) symmetry if possible, facilitates much more economical representation of an ODF using symmetry embedded GSH.  $\ddot{T}_l^{mn}$  are the functions incorporating solely crystal symmetries with no sample symmetries (triclinic textures). To fulfill, only  $\ddot{A}_l^{m\mu}$  coefficients are necessary in Eq. (7). While case studies presented in the paper will not consider any sample symmetry, the equations will be provided in a generalized way using symmetrized  $\ddot{T}_l^{\mu\nu}$ .

In order to evaluate the expansion coefficients,  $C_l^{\mu\nu}$ , the following orthogonality relation is used

$$\int_{\partial S} \ddot{T}_{l}^{\mu\nu}(g) \ddot{T}_{l}^{\nu\nu}(g) dg = \frac{1}{2l+1} \delta_{ll} \delta_{\mu\mu} \delta_{\nu\nu}, \text{ with } dg = \sin(\Phi) d\varphi_{1} d\Phi d\varphi_{2}.$$

$$\tag{8}$$

The asterisk (\*) symbol in the superscript indicates the complex conjugate. *dg* is the invariant orientation element of the Bunge-Euler OS. Multiplying with the complex conjugate, we have

$$\int_{CG} f(g) \ddot{T}_{l}^{*\mu\nu}(g) dg = \sum_{l=0}^{L} \sum_{u'=1}^{M(l)} \sum_{v'=1}^{N(l)} C_{l}^{\mu\nu} \int_{CG} \ddot{T}_{l}^{\mu\nu}(g) dg, \tag{9}$$

and then taking advantage of the orthogonality, we obtain

$$C_l^{\mu\nu} = (2l+1) \int_{OS} f(g) \dot{\vec{T}}_l^{*\mu\nu}(g) dg.$$
 (10)

 $C_l^{\mu\nu}$  represent a point in an infinite-dimensional Fourier space. The procedure for the compaction of an f(g) or ODF containing any number of crystal orientations is based on matching its GSH representation, Eq. (10), with those of another equivalent ODF by solving a nonlinear optimization problem in the space of expansion coefficients. We will refer to  $C_l^{\mu\nu}$  of the ODF we want to compact as the target texture point.

In our work, ODFs will be calculated from a set of *N* discrete orientations and weights indexed individually by k ( $\varphi_1^k, \Phi^k, \varphi_2^k, \alpha^k$ ) by averaging out the  $T_1^{i,\mu\nu}(g)$  from each orientation like

$$\widehat{C}_{l}^{\mu\nu} = \sum_{k=1}^{N} \dot{T}_{l}^{**\mu\nu} (\varphi_{1}^{k}, \Phi^{k}, \varphi_{2}^{k}) \frac{\alpha^{k}}{\sum_{l} \alpha^{l}}, \text{ with } C_{l}^{\mu\nu} = (2l+1)\widehat{C}_{l}^{\mu\nu}$$
(11)

Relying on  $C_l^{\mu\nu}$ ,  $f(g) = \sum_{l=0}^L \sum_{\mu=1}^{M(l)} \sum_{\nu=1}^{N(l)} C_l^{\mu\nu} T_l^{\mu\nu}$  is a continuous description of the probability density f(g) from a discrete set of orientations and their weights. We will begin using a shorthand expression for the probability density, where the subscript l is used to mean the index of  $l, \mu, \nu$  as

$$f(g) = \sum_{l} C_l \dot{T}_l. \tag{12}$$

This is done exclusively for convenience and simplicity.

We suitably define a scalar measure termed the texture difference index (*TDI*) to quantify the difference between any two textures. When the *TDI* is 0, it means the two textures are the same. When the *TDI* is one, the maximum, it means the two textures are as different as possible. The measure is redefined in the present work relative to the prior works as

$$TDI = \overline{T} \sum_{l} (\widehat{C}_{l} - \widehat{C}_{l})^{2}, \tag{13}$$

where  $\overline{T}$  is inverse of the maximum distance between two points in Fourier space calculated using the following equation

$$\overline{T} = \min \left[ \left( \sum_{l} (\widehat{C}_{l} - \widehat{C}_{l})^{2} \right)^{-1} \right], \tag{14}$$

where  $\widehat{C}$  and  $\widehat{C}_l$  are the expansion coefficients of single crystals meaning that the denuminator is fixed. Fig. 1 shows  $\overline{T}$  fits as functions of L for crystal symmetries.

# 2.2. Error, gradient, and Hessian for nonlinear optimization

The optimization is performed in Matlab using MathWorks' "Trust-Region-Reflective" fmincon solver. The function we are minimizing is

$$E = \sqrt{\sum_{l} \left( \left( \sum_{k} \dot{\bar{T}}_{l}^{k} \frac{\alpha^{k}}{\sum_{j} \alpha^{j}} \right) - \hat{C}_{l} \right)^{2}}, \tag{15}$$

where  $\dot{T}_l^k$  is a representation of each crystal in the compacted texture where k is the crystal index and l is the index of the Fourier Coefficient,  $\hat{C}_l$  is the target texture undergoing the compaction,  $\alpha^k$  is the volume fraction of each individual crystal, and the sum  $\sum_j \alpha^j$ 

over the crystals is used to normalize each  $\alpha^k$ . We manually normalize  $\alpha^k$  because the selected solver cannot have linear boundary constraints.

We substitute part of the error equation with  $G_l$  for clarity.

$$E = \sqrt{\sum_{l} G_{l}^{2}} \text{ with } G_{l} = \sum_{k} \dot{\tilde{T}}_{l}^{k} \frac{\alpha^{k}}{\sum_{j} \alpha^{j}} - \hat{C}_{l}.$$

$$(16)$$

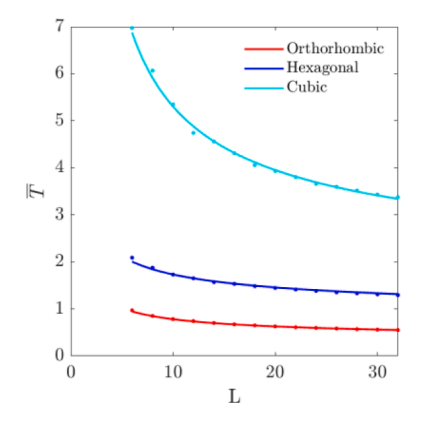
Evidently,  $G_l$  represents the difference between each index of  $\widehat{C}_l$  and the mean  $\dot{T}_l$  of the compacted texture. Since we have the objective function described analytically by a set of Fourier Coefficients, we can analytically calculate the gradient and Hessian matrix for efficient convergence. We find it ~300x faster than the implementation of Powell's Derivative Free Optimization Solvers. To calculate the gradient, we use the chain rule for each variable in the texture.  $x^m$  is used to indicate a variable that  $G_l$  depends on. There are four variables  $\varphi_1$ ,  $\Phi$ ,  $\varphi_2$ ,  $\alpha$  for each orientation used in the compaction. Therefore, the length of m is 4N, where N is the number of crystal orientations in the compacted set. It should be noted that the optimization methodology can be simplified to optimize only orientations,  $\varphi_1$ ,  $\Phi$ ,  $\varphi_2$ , or only weight,  $\alpha$ . However, the default option is to optimize a combination of both orientations and weights. We present the equations in such the most generic way. The gradient vector is calculated with respect to the variable indexed with m as

$$J(m') = \frac{\partial E}{\partial x^{m'}} = \frac{\partial \left(\sqrt{\sum_{l} G_{l}^{2}}\right)}{\partial x^{m'}} = \frac{\sum_{l} G_{l} \frac{\partial G_{l}}{\partial x^{m}}}{E}.$$
(17)

The Hessian as a symmetric square matrix is

$$H(m',n') = \frac{\partial E}{\partial x^{m'} \partial y^{n'}} = \frac{\left(\frac{\sum_{l} G_{l} \frac{\partial G_{l}}{\partial x^{m'}}}{E}\right)}{\partial y^{n'}} = \frac{\sum_{l} G_{l} \frac{\partial^{2} G_{l}}{\partial x^{m'} \partial y^{n'}} + \sum_{l} \frac{\partial G_{l}}{\partial y^{n'}} \frac{\partial G_{l}}{\partial x^{n'}} - \frac{\partial E}{\partial x^{m'}} \frac{\partial E}{\partial y^{n'}}}{E}$$

$$(18)$$



Crystal Symmetry	$\overline{T}$
Orthorhombic	$\frac{1}{0.4804*log(L+0.7646)+0.1382}$
Hexagonal	$\frac{1}{0.1601*log(L+0.2728)+0.2045}$
Cubic	$\frac{1}{0.1069*log(L+2.0585)-0.0776}$

Fig. 1. Normalization factor for obtaining TDI per crystal symmetry with no sample symmetry for different values of L along with the fits.

Evidently, the gradient and Hessian involve  $G_l$ ,  $\frac{\partial G_l}{\partial x^m}$ , and  $\frac{\partial^2 G_l}{\partial x^m}$ , which are provided in Appendix A. Having the gradient and the Hessian inserted into the "Trust-Region-Reflective" solver, a solution is continually updated until the error is satisfactorily low (10<sup>-10</sup>).

The procedure for compacting an ODF containing many either weighted or equally weighted crystal orientations finds an equivalent ODF containing a much smaller number of either weighted or not weighted crystal orientations. The procedure is developed and automated in Matlab (MathWorks, 2023). First, expansion coefficients of the ODF containing many orientations are calculated using to set the target point in the multidimensional Fourier space with coordinates  $C_l$  or  $\hat{C}_l$ . Next, to initiate the compaction procedure an initial guess containing N equally weighted crystal orientations is necessary to provide. The guess is created based on a set of 30,000 uniform orientations over the orientation space, each having a probability of  $f(g) = \sum_{l=0}^{L} \sum_{\mu=1}^{M(l)} \sum_{l=1}^{N(l)} C_l^{l\mu} \ddot{T}_l^{l\nu}$ . Note that the probability based on 30,000 crystal orientations corresponds exactly to the target  $C_l^{\mu\nu}$ . Then N crystal orientations are sampled from the probability. We would like to point out that the initial guess is not so important for our novel procedure because the procedure moves the orientations. However, finding a global optima would only be possible with a perfect guess. Finally, the optimization is run in Matlab to obtain a compacted ODF of N crystal orientations,  $\sum_{k=1}^{N} \ddot{T}_l^{ik} \frac{a^k}{\sum_{j}^{l} u^j}$ , which is equivalent to the target  $\hat{C}_l$ . The N crystal weights can be adjusted or not. The latter is a novel feature of the presented nonlinear optimization procedure compared to the old procedure reported

adjusted or not. The latter is a novel feature of the presented nonlinear optimization procedure compared to the old procedure reported in Eghtesad et al. (2018). The old procedure was based on a linear optimization of weights of a set of suitably selected crystal orientations obtained by binning of the Bunge-Euler orientation space or preferably by pre-fitting towards the target ODF using MTEX.

In the old procedure, beginning from the suitable set intended to represent the compact ODF, the linear programming problem was solved for weights of the expansion coefficients for each orientation to determine the compact ODF. The sum of the weighted coefficients of the compact ODF evolved during the solution procedure until matching the expansion coefficients of the target ODF. The linear optimization procedure was prone to failing because the selected crystal orientations were inadequate to achieve the solution. The expansion coefficients corresponding to the individual crystal orientations of the selected set make up a convex and compact region referred to as a hulls in the multidimensional Fourier space (Kalidindi et al., 2004; Knezevic and Kalidindi, 2007; Lyon and Adams, 2004; Wu et al., 2007). The hull is convex and compact because the space in between the points (the coefficients of single crystals) can be filled by combination of the points linearly. To solve the linear programing problem for weights, the target point of coefficients corresponding to the target ODF must have been contained within the hull. In another words, the solution was available if the target point was within the hull of the compact ODF. Given that this was not always the case in every dimension of the space, another set of crystals need to be selected. Therefore, the procedure had to iterate multiple times for selecting crystal orientations to eventually optimize their weights during the solution procedure. Adjusting the crystal orientations during the solution procedure is an essential feature of the novel procedure presented in this paper. The concept of hull is not needed in the new procedure.

The number of dimensions used in the fitting procedure is determined by L. The accuracy of the representation and the computational time involved in the procedure scale with L. The number of dimensions to fit depends on L. The numbers of dimensions for L = 8, L = 16, and L = 32 relevant in the present work are 39, 205, and 1253 for triclinic-cubic, 74, 377, and 2420 for triclinic-hexagonal,

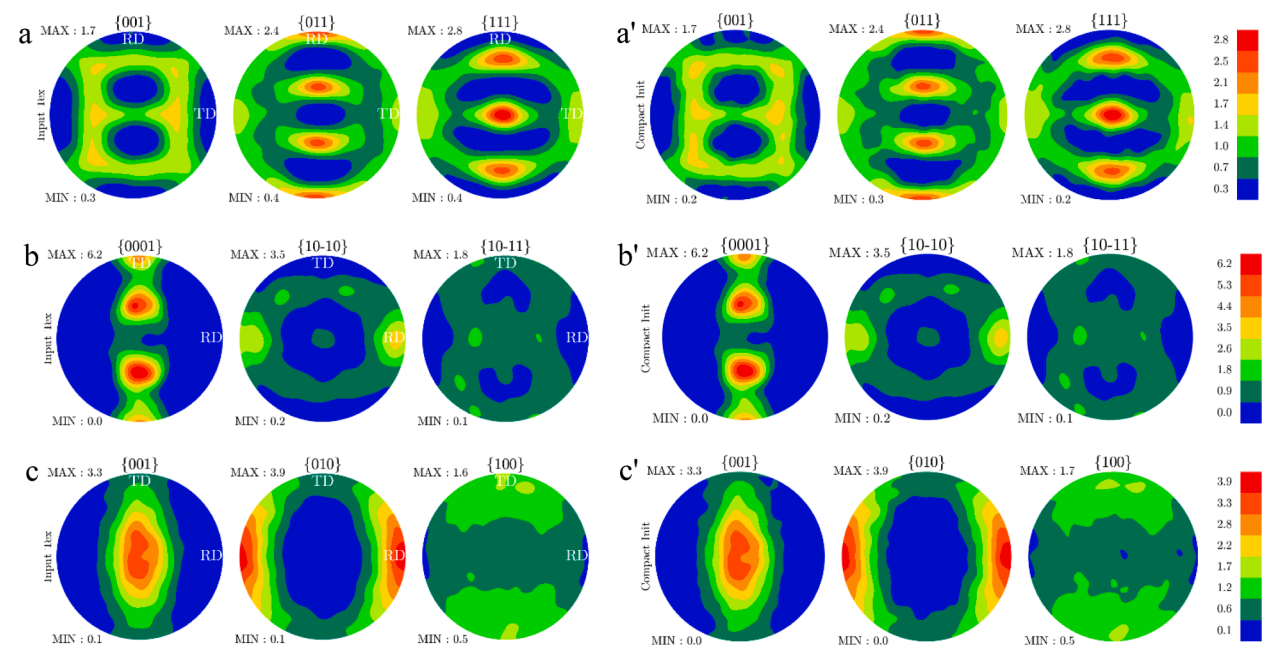


**Fig. 2.** Stereographic pole figures comparing the measured full size texture (left, a, b, c) and compacted texture (right a', b', c') for (a, a') AA6016-T4, and (b, b') pure Ti, and (c, c') U. These textures are used to initialize crystal plasticity simulations.

and 174, 1004, and 6680 for triclinic-orthorhombic. The first frequency, which is always (Re = 1, Im = 0) was not counted. Note that TDI was always calculated with L = 32. The previous linear optimization procedure had difficulties fitting L > 8, especially for the low crystal symmetries. The procedure was set to cycle for another ODF with the same or increased number of discrete orientation or for a lower L in case it fails to fit the desired number of dimensions. The novel procedure can fit any L. The novel procedure is applied to several case studies as presented and discussed in the next section.

#### 3. Results

Three materials, one cubic, one hexagonal, and one orthorhombic are selected to show the utility of the developed procedure. The

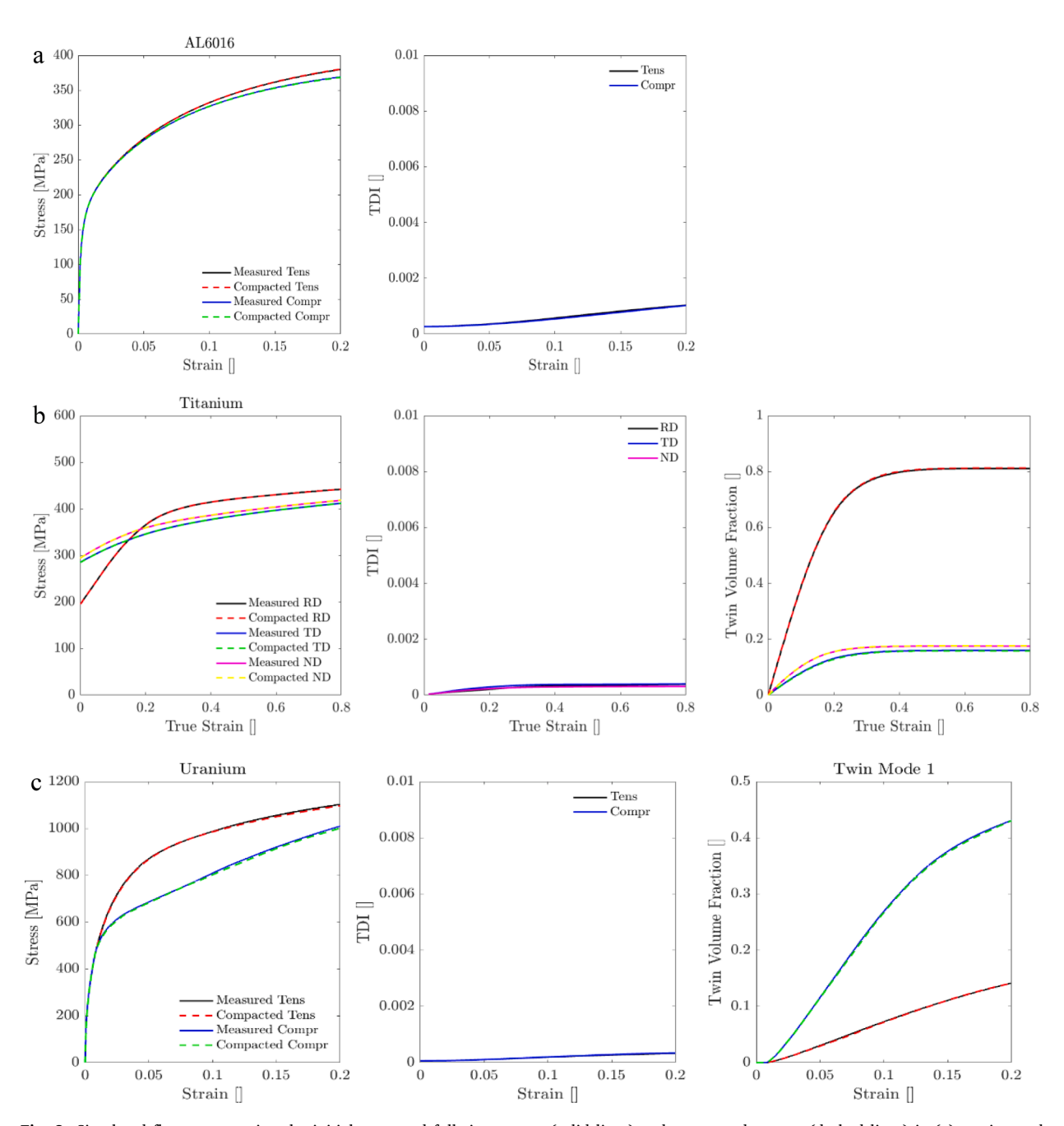


**Fig. 3.** Simulated flow curves using the initial measured full size texture (solid lines) and compacted texture (dashed lines) in (a) tension and compression along TD of AA6016-T4, and (b) compression along RD, TD and ND of pure Ti, and (c) tension and compression of U. The evolution of *TDI* between the full-size texture and compacted texture during deformation. The evolution of twinning during deformation.

case studies are of different complexity owing to different crystal structures ranging from simple cubic to more complex hexagonal to the most complex low symmetry orthorhombic aimed at fully validating the developed procedure. The cubic material is an Al alloy (AA) 6016-T4 in the form of an as-received rolled sheet. The texture of the sheet was measured by neutron diffraction. Such measurement technique measures macro-texture. An ODF containing 5000 weighted crystal orientations was reconstructed from the

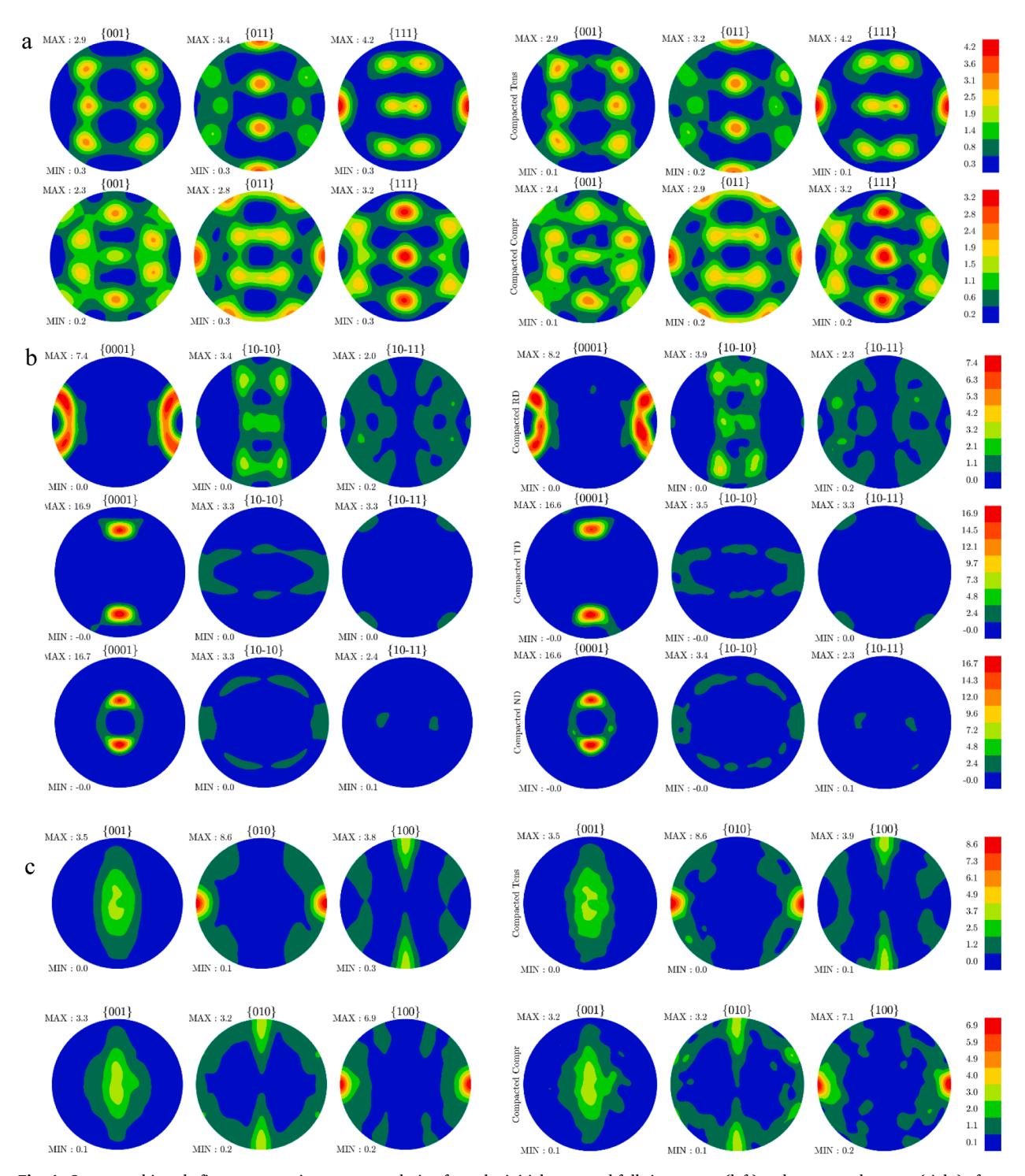


**Fig. 4.** Stereographic pole figures comparing texture evolution from the initial measured full size texture (left) and compacted texture (right) after (a) tension and compression along TD of AA6016-T4, and (b) compression along RD, TD and ND of pure Ti, and (c) tension and compression of U. These pole figures are in the same frame as the initial measured pole figures per structure in Fig. 2.

measured data. Pole figures showing the measured texture are presented in Fig. 2a. The hexagonal material is a rolled plate of high purity Ti (Savage et al., 2021). The texture of the plate was measured using electron backscattered diffraction (EBSD). Such measurement technique measures micro-texture. The file contained about 500,000 equally weighted orientations. Pole figures showing the measured texture of pure Ti are presented in Fig. 2b. Finally, the orthorhombic material is a straight rolled uranium (U) (Knezevic et al., 2012). The texture was measured using EBSD containing about 80,000 equally weighted orientations. Pole figures showing the measured texture of U are presented in Fig. 2c. The compaction of the three target ODFs is performed to L=32 using the novel procedure. Pole figures of the compacted textures are presented in (a') for AA6016-T4, (b') for pure Ti, and (c') for U and these are essentially indistinguishable from the pole figures showing the corresponding full textures. The compacted texture of AA6016-T4 contained 100 weighted crystal orientations, that for pure Ti contained 200 weighted crystal orientations, while that for U contained 400 weighted crystal orientations.

Texture evolves during plastic deformation because of plastic shearing on slip systems and reorientations due to twinning. Crystal plasticity models have been developed to capture the texture evolution and resulting anisotropic mechanical response of polycrystalline metals. These models consider the operating crystallographic slip and twinning deformation mechanisms. The cubic metal deforms by an octahedral  $\{110\}\langle \overline{1}11\rangle$  slip mode. The hexagonal metal deformed by prismatic  $\{1\overline{1}00\}\langle 11\overline{2}0\rangle$ , basal  $\{0001\}\langle \overline{2}110\rangle$ , and pyramidal  $\{10\overline{1}1\}\langle 2\overline{113}\rangle$  slip modes and twinning  $\{10\overline{1}2\}\langle \overline{1}011\rangle$  and  $\{11\overline{2}2\}\langle 11\overline{23}\rangle$ . Finally, the orthorhombic metal deforms by wall (010)[100], chimney  $\{110\}<1\overline{1}0>$ , floor (001)[100], and roof  $\{021\}<1\overline{1}2>$  slip modes and twinning  $\{130\}<3\overline{1}0>$  and  $\{172\}<3\overline{1}2>$ . Fig. 3 shows simulated flow stress response in quasi-static tension and compression along the sheet transverse direction (TD) for AA6016-T4 using EPSC (Daroju et al., 2022), quasi-static compression along the plate rolling direction (RD), TD, and normal direction (ND) for pure Ti using VPSC (Savage et al., 2021), and quasi-static tension and compression along RD for U using EPSC (Barrett et al., 2020; Knezevic et al., 2012) based on the initial full and compacted textures. The provided references per case study describe details pertaining to the crystal plasticity models used in the simulations. Evidently, the calculated flow curves based on the full and compacted ODFs are nearly identical. Given that pure Ti and U deform by twinning, the figure also shows the predicted twin volume fractions. Finally, the figure shows the evolution of TDI between the full and compacted ODFs during deformation. The TDI measure is used to quantify the differences in the texture evolution between the full and compacted ODFs. Evidently, the compact ODF is sufficient to capture flow stress response, texture evolution, and twinning evolution to large strains not appreciably different from the full ODF for each case study. Fig. 4 shows pole figures visualizing the predicted textures based on the full and compacted initial ODFs at the end of deformation for each case study.

#### 4. Discussion

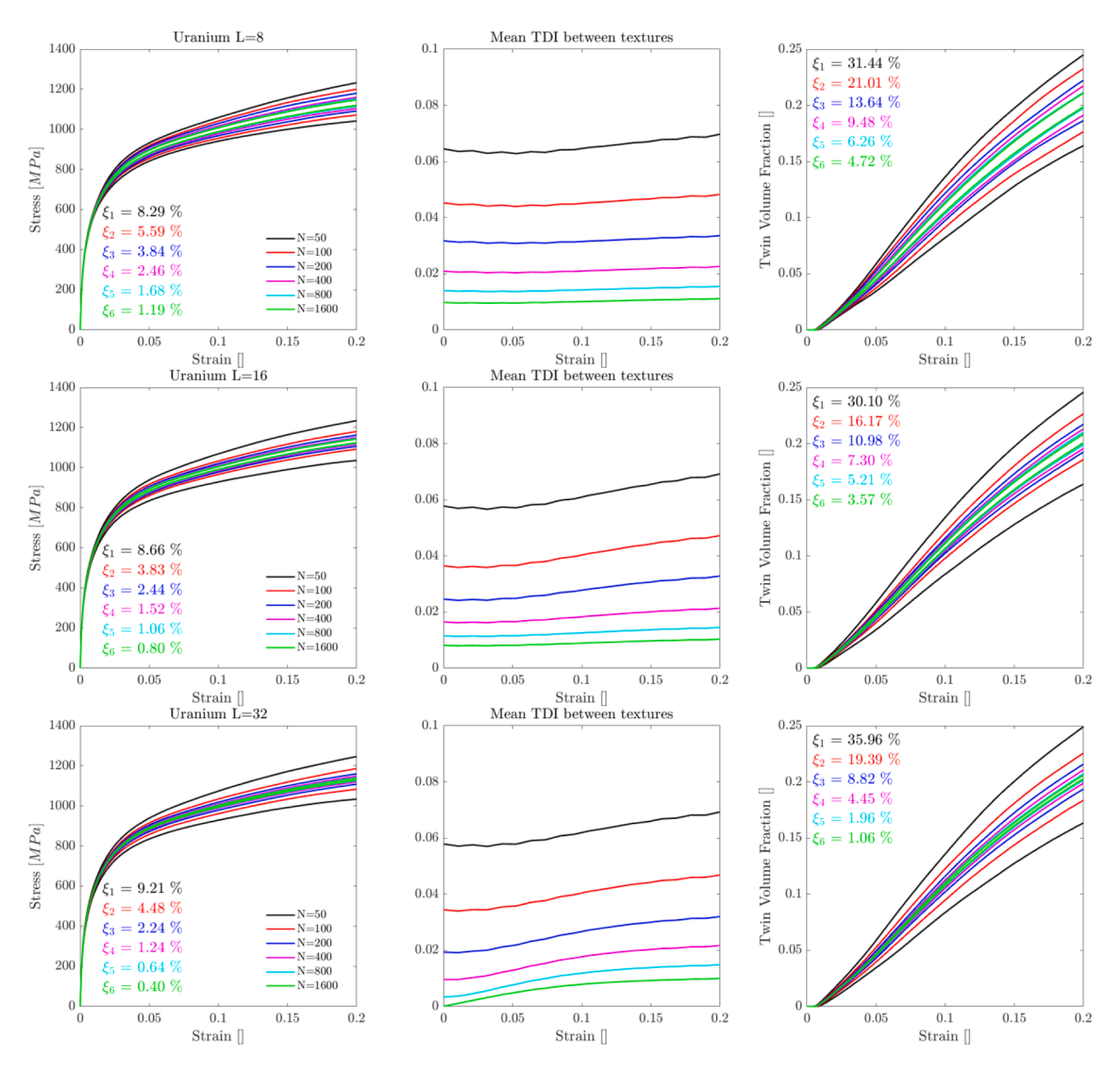
The procedure developed in the present paper constitutes a rigorous methodology for the compaction of crystallographic texture data aimed to improve the efficiency of crystal plasticity models, especially those coupled with the finite element method computational tools. The computational time involved in crystal plasticity simulations scales linearly with the number of crystal orientations. The speedups are therefore directly proportional to the reduction in the number of crystal orientations representing texture. The developed compaction methodology is an essential contribution to enable future large scale crystal plasticity finite element simulations of deformation processes.

The procedure can compact any statistical ODF containing any number of crystal orientations weighted or not to an equivalent but compact ODF containing a much smaller number of crystal orientations also weighted or not as desired. Moreover, weights can be preset for *N* orientations for the procedure to find the orientations that would fit a given full size ODF. This is particularly useful if attempting to couple the developed procedure with the digital representation environment for the analysis of microstructure in 3D (Dream. 3D) software (Groeber et al., 2008; Groeber and Jackson, 2014). To this end, grains synthetized in Dream.3D would have certain volumes. The GSH representation and the linearity of the expansion space enabled the development of the procedure. Accuracy and utility of the procedure was demonstrated by predicting the evolution of flow stress, texture, and twinning for AA6016-T4, pure Ti, and U. The case studies showed that the compact ODFs can capture every aspect of deformation behavior with great accuracy just like the full ODFs.

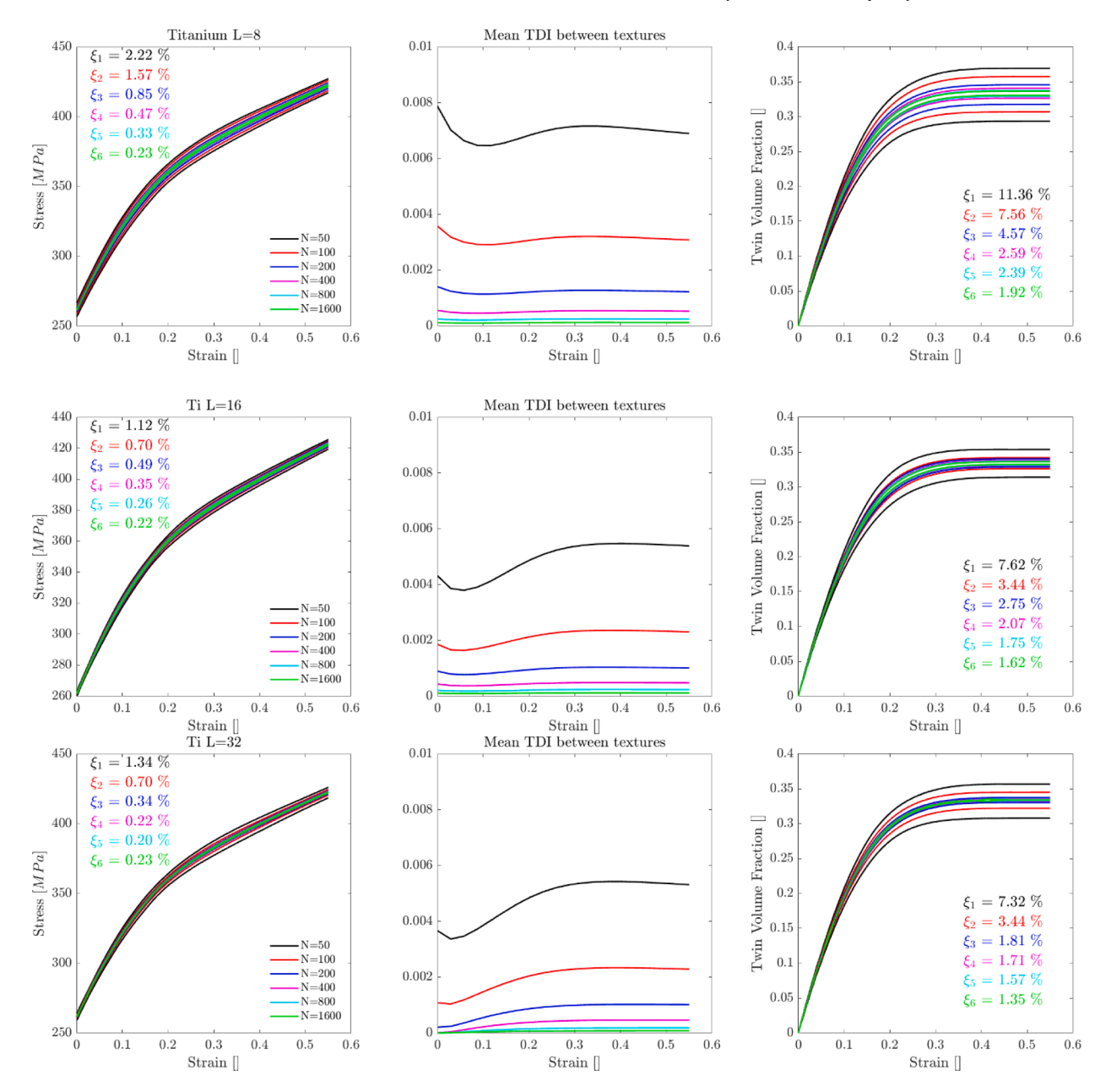
In closing, we present guidance for selecting optimal number of crystal orientations for crystal plasticity simulations trading off the accuracy of the compaction and the benefits in improving the computational speed. In doing so, we further verify the procedure by compacting the same texture many different times from a different initial guess. We check if the crystal plasticity models predict consistent outputs for six sets of 200 different ODFs representing the same target ODF taken to be a uniform ODF with different number of crystal orientations. The uniform is taken as a target since it is the most challenging to fit. The procedure for creating the six sets of 200 as different as possible textures per crystal structure containing 50, 100, 200, 400, 800, and 1600 crystal orientations per set is described in Appendix B. Each set of the initial guess textures,  $\hat{C}_l^z$  with z=1,2,... 200, fits the same target,  $\hat{C}_l$ , using the developed fitting procedure with adjusting weights and orientations and with adjusting orientations solely. We obtain sets of six two times. This is to check if there is any difference in accuracy if the fitting is done by adjusting weights and orientations or with adjusting orientations solely. Note that the latter can be equally weighted orientations or weighted orientations, but their weights would not be changed during the fitting. Typically, adjusting orientations solely requires more iterations but size of the arrays and matrices is smaller (3/4). The fitting was performed up to L=8, L=16, and L=32. Pole figures for the 200 textures look nearly the same, especially for N>100. While we create textures with nearly identical pole figures, the purpose is to evaluate whether these textures govern the same or similar material properties. We reiterate that each set of 200 textures has either 50 or 100 or 200 or 400 or 800 or 1600 crystal orientations.

Fig. 5 presents the results of the parametric study in terms of the predicted min and max flow stress curves and min and max twin

volume fractions for U amongst the 200 runs of compression along RD using 200 input textures with adjusted weights and orientations to fit the same target. Fig. 6 presents the results of the parametric study in terms of the predicted min and max flow stress curves and min and max twin volume fractions for pure Ti amongst the 200 runs of compression along RD using 200 input textures with adjusted weights and orientations to fit the same target. Finally, Fig. 7 presents the results of the parametric study in terms of the predicted min and max flow stress curves for AA6016-T4 amongst the 200 runs of compression along TD using 200 input textures with adjusted weights and orientations to fit the same target. Appendix C provides the same plots as those in Figs. 5–7 but based on textures with adjusting orientations solely to fit the same target. The legends in the flow stress figures approximate the error of the procedure per *N*. The error is conveniently defined as the maximum standard deviation of stress at each strain increment normalized by the average stress at each increment as  $\xi = 3\max\left(\frac{std(x_i)}{\bar{x}_i}\right)$ . Similarly, the legends in the twin volume fractions plots specify the maximum standard



**Fig. 5.** The softest (minimum) and the strongest (maximum) flow stress curves amongst the 200 simulations of compression along RD for U initialized using 200 as different as possible initial textures fit to the same target. Six sets of 200 textures varied in the number of crystal orientations N, as specified in the legend. The fitting was done by adjusting weights and orientations for L = 8 (top row), L = 16, and L = 32 (bottom row). The other legends specify the maximum standard deviation of stress over strain increment normalized by the average stress at the given increment. The evolution of mean TDI with strain for given N. The smallest (minimum) and the highest (maximum) twin volume fraction amongst the 200 simulations. The legends specify the maximum standard deviation of twinning over the strain increment normalized by the average value at the given increment.



**Fig. 6.** The softest (minimum) and the strongest (maximum) flow stress curves amongst the 200 simulations of compression along RD for pure Ti initialized using 200 as different as possible initial textures fit to the same target. Six sets of 200 textures varied in the number of crystal orientations N, as specified in the legend. The fitting was done by adjusting weights and orientations for L = 8 (top row), L = 16, and L = 32 (bottom row). The other legends specify the maximum standard deviation of stress over strain increment normalized by the average stress at the given increment. The evolution of mean TDI with strain for given N. The smallest (minimum) and the highest (maximum) twin volume fraction amongst the 200 simulations. The legends specify the maximum standard deviation of twinning over the strain increment normalized by the average value at the given increment.

deviation of twinning over the strain increment normalized by the average value at the given increment. The Figs. 5–7 also present the evolution of *TDI* with strain. An average *TDI* between every of the 200 textures as they evolve is calculated and plotted. The number of possibilities (combinations) to obtain the mean is 200 choose 2, which is 19,900. Evidently, the error reduces with *N*.

U as a highly anisotropic material owing to its low symmetry structure best reveals the error. The simulations show a significant difference in the predictions based on a set of 200 different input textures up to N=400. The differences are the greatest when the fitting was performed using L=8, while the fitting using L=16 and L=32 produces similar differences. It is worth reflecting on that the EDAX OIM (orientation imaging microscopy) analyses software, TSL (TexSEM Laboratories), uses the default value of L as L=16 (EDAX and TSL, 2024). Moreover, the representation of ODF-elastic stiffness relationships requires L=4, while the representation of

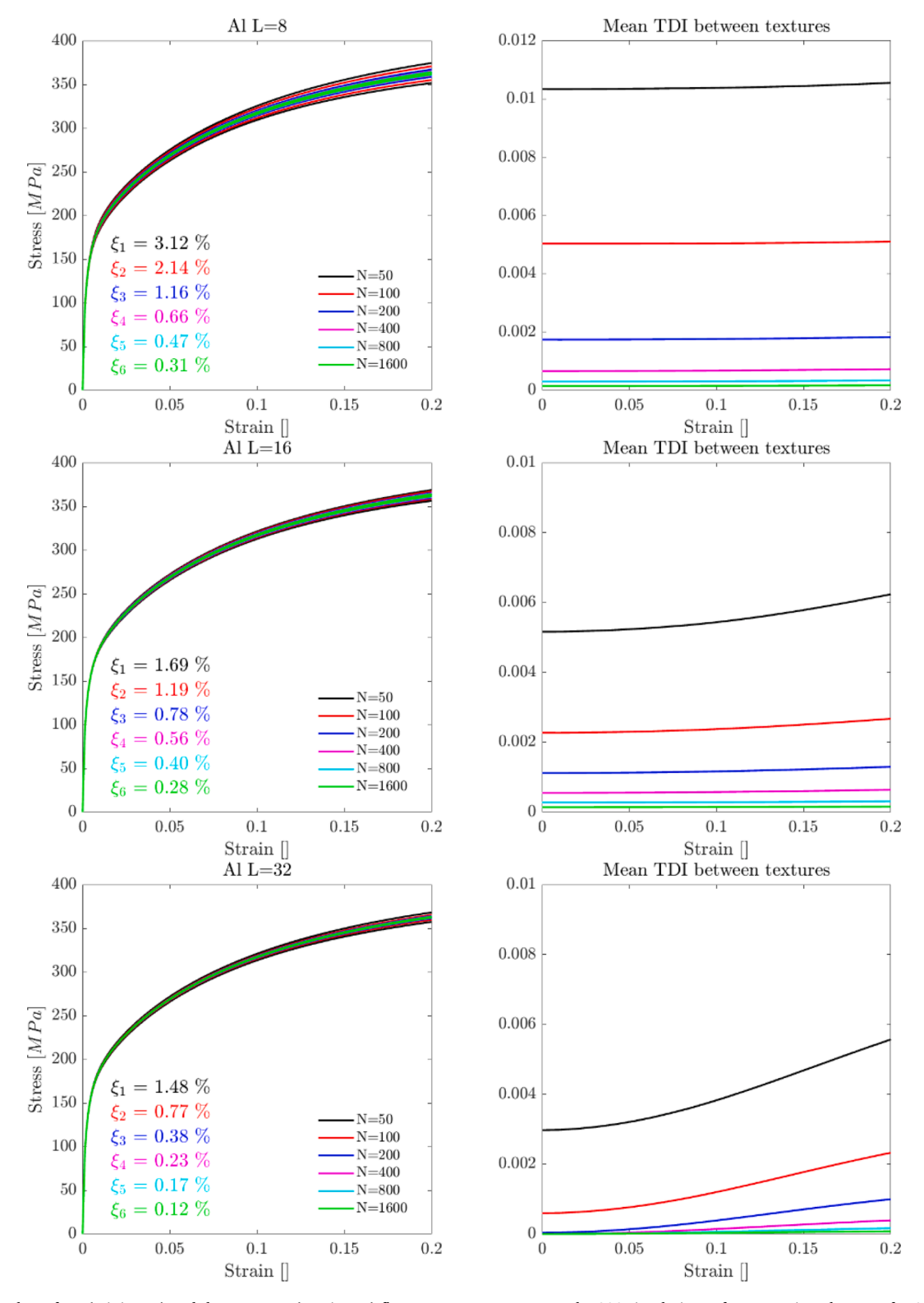


**Fig. 7.** The softest (minimum) and the strongest (maximum) flow stress curves amongst the 200 simulations of compression along TD for AA6016-T4 initialized using 200 as different as possible initial textures fit to the same target. Six sets of 200 textures varied in the number of crystal orientations N, as specified in the legend. The fitting was done by adjusting weights and orientations for L = 8 (top row), L = 16, and L = 32 (bottom row). The other legends specify the maximum standard deviation of stress over strain increment normalized by the average stress at the given increment. The evolution of mean TDI with strain for given N.

ODF-yield stress requires L to about 10 or 12 (Fast et al., 2008; Knezevic and Kalidindi, 2007; Shaffer et al., 2010). However, the representation of texture is more demanding than the representation of properties using the GSH basis. The results show that N = 400 and L = 16 is sufficiently accurate for U. Looking at the results in Appendix C, we observe that adjusting orientations solely or adjusted weights and orientations produces similar results. Slightly greater compaction can be achieved by adjusted weights and orientations. Hexagonal metals and especially cubic metals can be fit with lower number of orientations. N = 200 is sufficient for pure Ti, while N = 100 is sufficient for AA6016-T4.

#### 5. Conclusions

Metal forming process simulations using the finite elements method with crystal plasticity constitutive laws are impractical in part because of the need to store many state variables because of many crystal orientations embedded at integration points. The computational time scales nearly linear with the number of crystal orientations embedded at integration points because the crystal plasticity equations must be solved for stress for every crystal in every trial increment. This work successfully developed a nonlinear optimization procedure for compacting input ODFs in crystal plasticity codes to contain computationally manageable quantities of crystal orientations. The core of the procedure is the spectral representation of ODFs using the GSH basis. Specifically, the spectral representation of a full size ODF containing many crystal orientations is matched with the spectral representation of an ODF containing a compact set of orientations. The gradient vector and the Hessian matrix are derived analytically for rapid convergence of the procedure relying on the Matlab optimization solver. The procedure can compact any statistical ODF containing either weighted or not weighted crystal orientations into an equivalent but compact ODF containing also weighted or not weighted crystal orientations as desired. Case studies involving metals with cubic, hexagonal, and orthorhombic crystal structures revealed that the flow curves, texture evolution, and twinning can be predicted nearly identically using the compacted ODFs as using the full size ODFs. The parametric study performed to guide selecting optimal number of crystal orientations for crystal plasticity simulations trading off the accuracy of the compaction and the benefit in improving the computational speed suggests that 400 crystal orientations are sufficient to accurately represent textures of orthorhombic metals, 200 crystal orientations to accurately represent textures of hexagonal metals, and 100 crystal orientations to accurately represent textures of cubic metals. We anticipate that the developed procedure will become an essential tool for compacting input ODFs in many future metal forming process simulations involving crystal plasticity constitutive laws.

#### Data availability

The achieved git repository associated with this work can be found at https://github.com/russellemarki/TextureReduction.

# CRediT authorship contribution statement

Russell E. Marki: Formal analysis, Investigation, Methodology, Software, Validation, Visualization. Marko Knezevic: Conceptualization, Methodology, Investigation, Project administration, Resources, Supervision, Writing – original draft, Writing – review & editing, Funding acquisition.

# Declaration of competing interest

The authors declare that they have no known competing financial interests or personal relationships that could have appeared to influence the work reported in this paper.

# Acknowledgments

This work is based upon a project sponsored by the U.S. National Science Foundation under grant no. CMMI- 2147122.

# Appendix A

This appendix defines  $\frac{\partial G_1}{\partial x^m}$  and  $\frac{\partial^2 G_1}{\partial x^m}$  necessary for obtaining the gradient vector and Hessian matrix. The most essential constituent are the derivatives of Eq. (4). The derivatives are with respect to  $\varphi_1$ ,  $\Phi$ ,  $\varphi_2$ , and  $\alpha$ , which are embedded into the  $x^m$  vector. However,  $\varphi_1$ ,  $\Phi$ , and  $\varphi_2$  individually are represented by  $\varphi$  and  $\Phi$  in the equations that follow, while  $\alpha$  is separated. As a result, we switch from m enumerating N length to m enumerating N length to allow us to represent the derivatives as a function of orientation conveniently. The derivatives with respect to  $\varphi$  and  $\Phi$  are therefore vectors of N length, while the derivative with respect to  $\alpha$  are vectors of N length appended to the former N length vector to obtain the N length. Note that all have an extra dimension, which is the number of Fourier coefficients. The derivatives are (no summations on m)

$$\frac{\partial G_l}{\partial \varphi^m} = \frac{\partial \ddot{T}_l^m}{\partial \varphi^m} \frac{\alpha^m}{\sum_i \alpha^i} \tag{A1}$$

$$\frac{\partial G_l}{\partial \alpha^m} = \frac{\dot{T}_l^m - \hat{C}_l - G_l}{\sum_{i} \alpha^j}$$
(A2)

$$\frac{\partial^2 G_l}{\partial \varphi^m \partial \Phi^m} = \frac{\partial^2 \dot{T}_l^m}{\partial \varphi^m \partial \Phi^m} \frac{\alpha^m}{\sum_{i:} \alpha^i}$$
(A3)

$$\frac{\partial^2 G_l}{\partial \alpha^n \partial \varphi^m} = \frac{\delta_{mn} \frac{\partial \dot{T}_l^m}{\partial \varphi^m} - \frac{\partial G_l}{\partial \varphi^m}}{\sum_i \alpha^i}$$
(A4)

$$\frac{\partial^2 G_l}{\partial \alpha^m \partial \alpha^n} = \frac{-\frac{\partial G_l}{\partial \alpha^m} - \frac{\partial G_l}{\partial \alpha^n}}{\sum_{i} \alpha^j} \tag{A5}$$

# Appendix B

This appendix presents equations pertaining to calculating as different as possible initial textures used in the parametric study presented in Section 4. Beginning from a uniform texture, the methodology adds another texture as different as possible from the existing one. The uniform texture is  $\widehat{C}_l^z$  (total z of one) containing N number of equally weighted crystal orientations.  $\widehat{C}_l^1$  is used in the equations that follow to construct a new different texture,  $\widehat{C}_l^2$  (now a total z of two), which is set to also contain N equally weighted crystal orientations. Next, the methodology adds another texture as different as possible from the existing two. Repeat this process until  $\widehat{C}_l^z$  has (200 + 1) total textures to obtain a sought set of 200 different textures, excluding the initial uniform,  $\widehat{C}_l^1$ .

The optimization procedure is conceived to keep adding textures with the highest minimum distance from the nearest texture that already exists in the set one at a time. The distance is

$$D = \left(\sum_{l} E_{z}^{r}\right)^{\frac{1}{l}} \text{ with } E_{z} = \sqrt{\sum_{l} \left(\sum_{k} \dot{\tilde{T}}_{l}^{k} \frac{\alpha^{k}}{\sum_{j} \alpha^{j}} - \hat{C}_{l}^{z}\right)^{2}}$$
 (B1)

The higher the exponent r, the closer D will be to the actual maximum distance but the equations exhibit steeper derivatives and slower convergence. In our optimization for obtaining sets of 200 different textures, we have set r=15. Sets of 200 textures containing 50, 100, 200, 400, 800, and 1600 crystal orientations per set are created. It remains to define  $\frac{\partial D}{\partial \omega m}$  and  $\frac{\partial^2 D}{\partial \omega m \partial \omega m}$  for Matlab's fminunc as

$$\frac{\partial D}{\partial \varphi^m} = \left(\sum E_z^r\right)^{\frac{1}{r}-1} \sum_z \left(\frac{\partial E_z}{\partial \varphi^m} E_z^{r-1}\right) \text{ with } \frac{\partial E_z}{\partial \varphi^m} = \sum_l \left(\frac{\partial \ddot{T}_l^m}{\partial \varphi^m} \frac{\alpha^m}{\sum_l \alpha^l} G_l^z\right) \text{ and } G_l^z = \widehat{C}_l - \widehat{C}_l^z$$
(B2)

$$\frac{\partial^2 D}{\partial \varphi^m \partial \varphi^n} = \left(\sum E_z^r\right)^{\frac{1}{r}-1} \left(\sum_z E_z^{r-2}\right) \sum_l \left(\frac{\partial \overset{\cdot}{T}_l^m}{\partial \varphi^m} \frac{\partial \overset{\cdot}{T}_l^n}{\partial \varphi^n} \frac{\alpha^m \alpha^n}{\sum_j \alpha^j \sum_j \alpha^j}\right) + (r-2) \left(\sum E_z^r\right)^{\frac{1}{r}-1} \sum_z \left(E_z^{r-2} \frac{\partial E_z}{\partial \varphi^m} \frac{\partial E_z}{\partial \varphi^n}\right) + (r-2) \left(\sum E_z^r\right)^{\frac{1}{r}-1} \sum_z \left(E_z^{r-2} \frac{\partial E_z}{\partial \varphi^m} \frac{\partial E_z}{\partial \varphi^n}\right) + (r-2) \left(\sum E_z^r\right)^{\frac{1}{r}-1} \sum_z \left(E_z^{r-2} \frac{\partial E_z}{\partial \varphi^m} \frac{\partial E_z}{\partial \varphi^n}\right) + (r-2) \left(\sum E_z^r\right)^{\frac{1}{r}-1} \sum_z \left(E_z^{r-2} \frac{\partial E_z}{\partial \varphi^m} \frac{\partial E_z}{\partial \varphi^n}\right) + (r-2) \left(\sum E_z^r\right)^{\frac{1}{r}-1} \sum_z \left(E_z^{r-2} \frac{\partial E_z}{\partial \varphi^m} \frac{\partial E_z}{\partial \varphi^n}\right) + (r-2) \left(\sum E_z^r\right)^{\frac{1}{r}-1} \sum_z \left(E_z^{r-2} \frac{\partial E_z}{\partial \varphi^m} \frac{\partial E_z}{\partial \varphi^n}\right) + (r-2) \left(\sum E_z^r\right)^{\frac{1}{r}-1} \sum_z \left(E_z^{r-2} \frac{\partial E_z}{\partial \varphi^m} \frac{\partial E_z}{\partial \varphi^n}\right) + (r-2) \left(\sum E_z^r\right)^{\frac{1}{r}-1} \sum_z \left(E_z^{r-2} \frac{\partial E_z}{\partial \varphi^m} \frac{\partial E_z}{\partial \varphi^n}\right) + (r-2) \left(\sum E_z^r\right)^{\frac{1}{r}-1} \sum_z \left(E_z^{r-2} \frac{\partial E_z}{\partial \varphi^m} \frac{\partial E_z}{\partial \varphi^m}\right) + (r-2) \left(\sum E_z^r\right)^{\frac{1}{r}-1} \sum_z \left(E_z^r\right)^{\frac{1}{r}-1} \sum_z \left($$

$$+\frac{1-r}{D}\frac{\partial D}{\partial \varphi^m}\frac{\partial D}{\partial \varphi^n} + \left(\sum E_z^r\right)^{\frac{1}{r-1}} \sum_z \left(\sum_l \left(\frac{\partial^2 \dot{T}_l^m}{\partial \varphi^m \partial \Phi^m} \frac{\alpha^m}{\sum_l \alpha^l} G_l^z\right) E_z^{r-1}\right)$$
(B3)

Note that the derivatives do not depend on  $\widehat{C}_l^z$ , and that an added texture is  $\widehat{C}_l = \sum_k \dot{T}_l^t \frac{\alpha^k}{\sum_j \sigma^l}$ . We only optimized  $\varphi$  when creating different textures.

# Appendix C

This appendix shows the same plots as those in Figs. 5–7 in Figs. C1–C3 but based on the textures fitted to the same target by adjusting orientations solely.

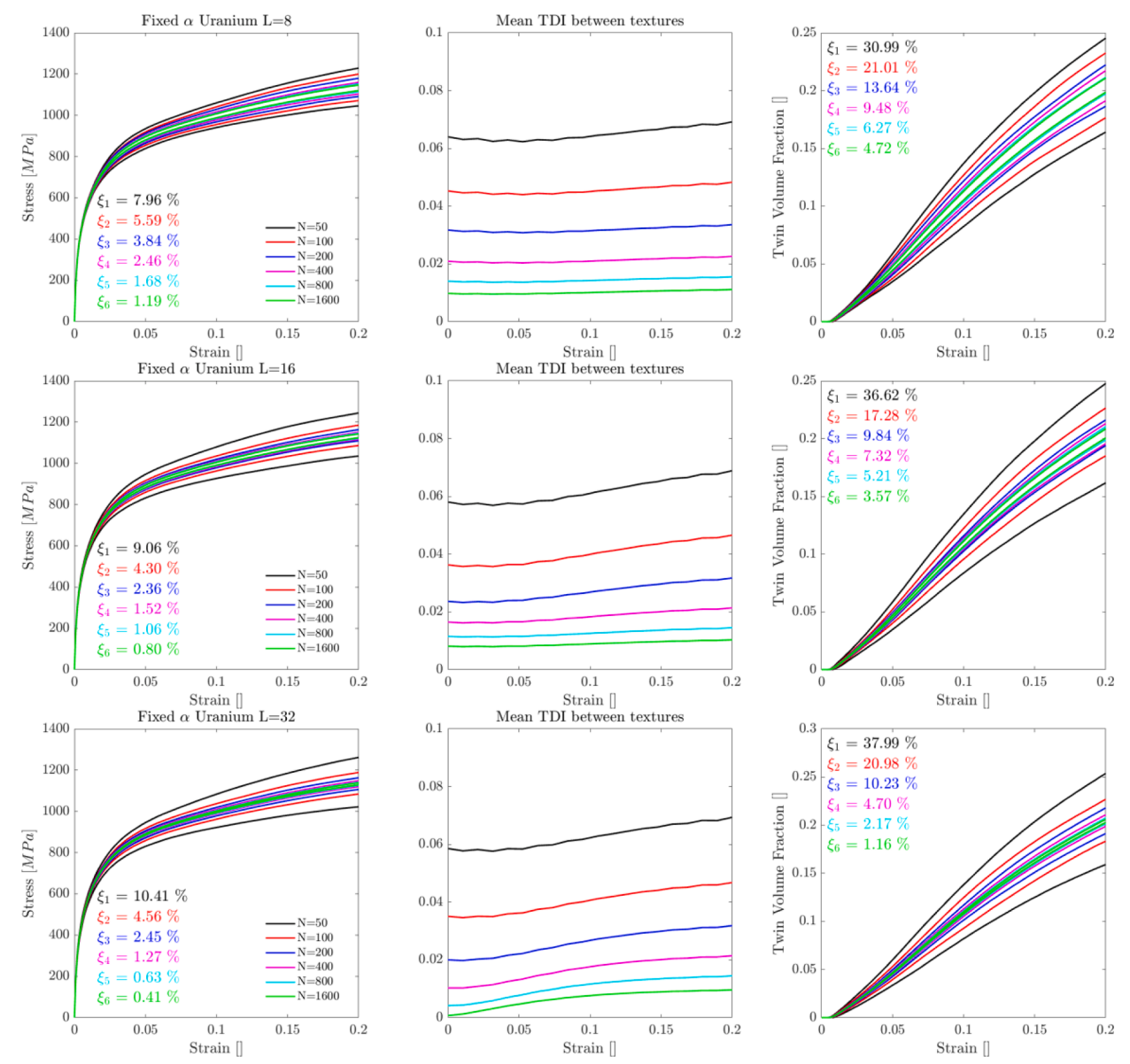


Fig. C1. The same as Fig. 5 but based on 200 textures with adjusted orientations (fixed weights) to the same target.

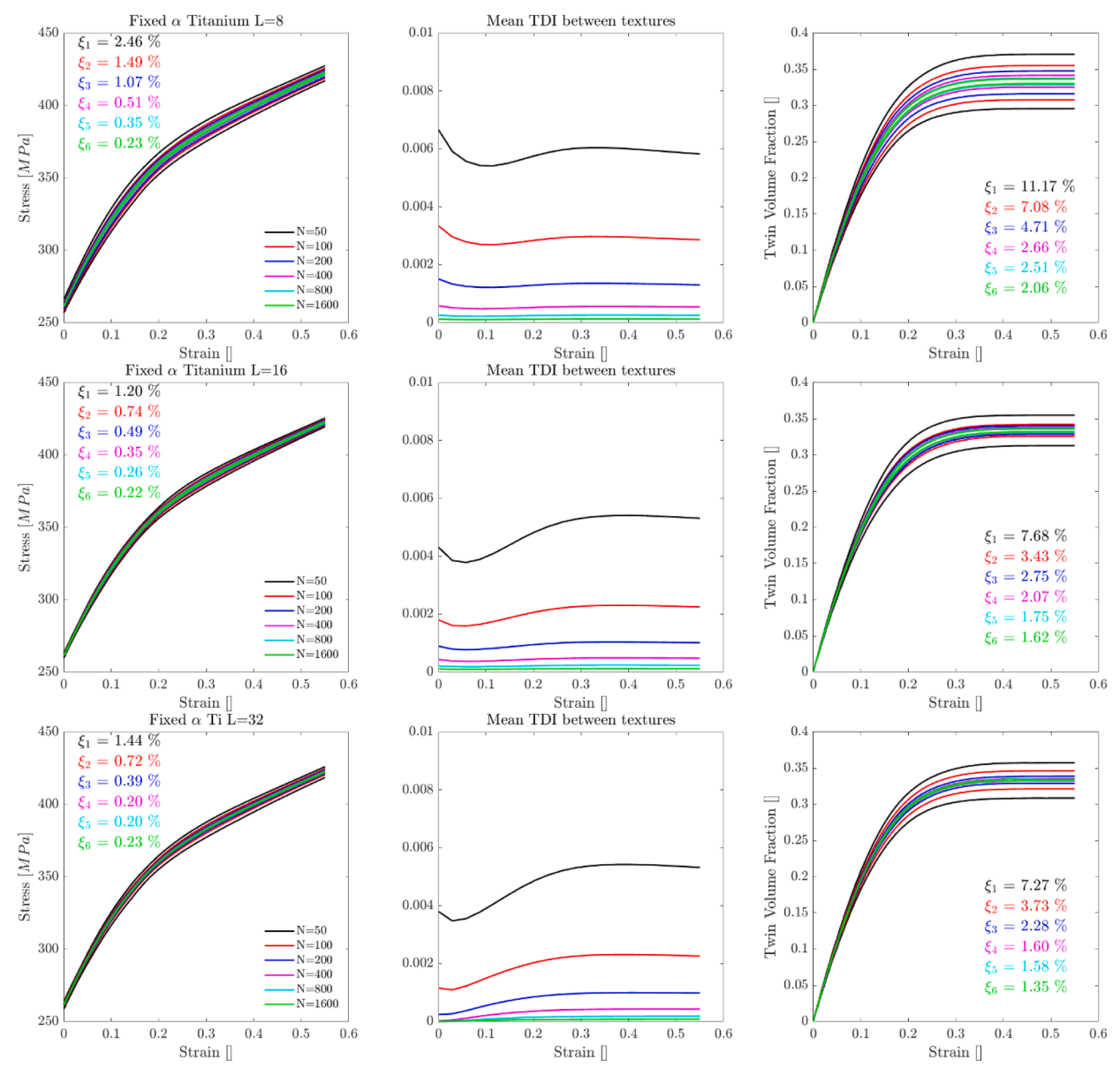


Fig. C2. The same as Fig. 6 but based on 200 textures with adjusted orientations (fixed weights) to the same target.

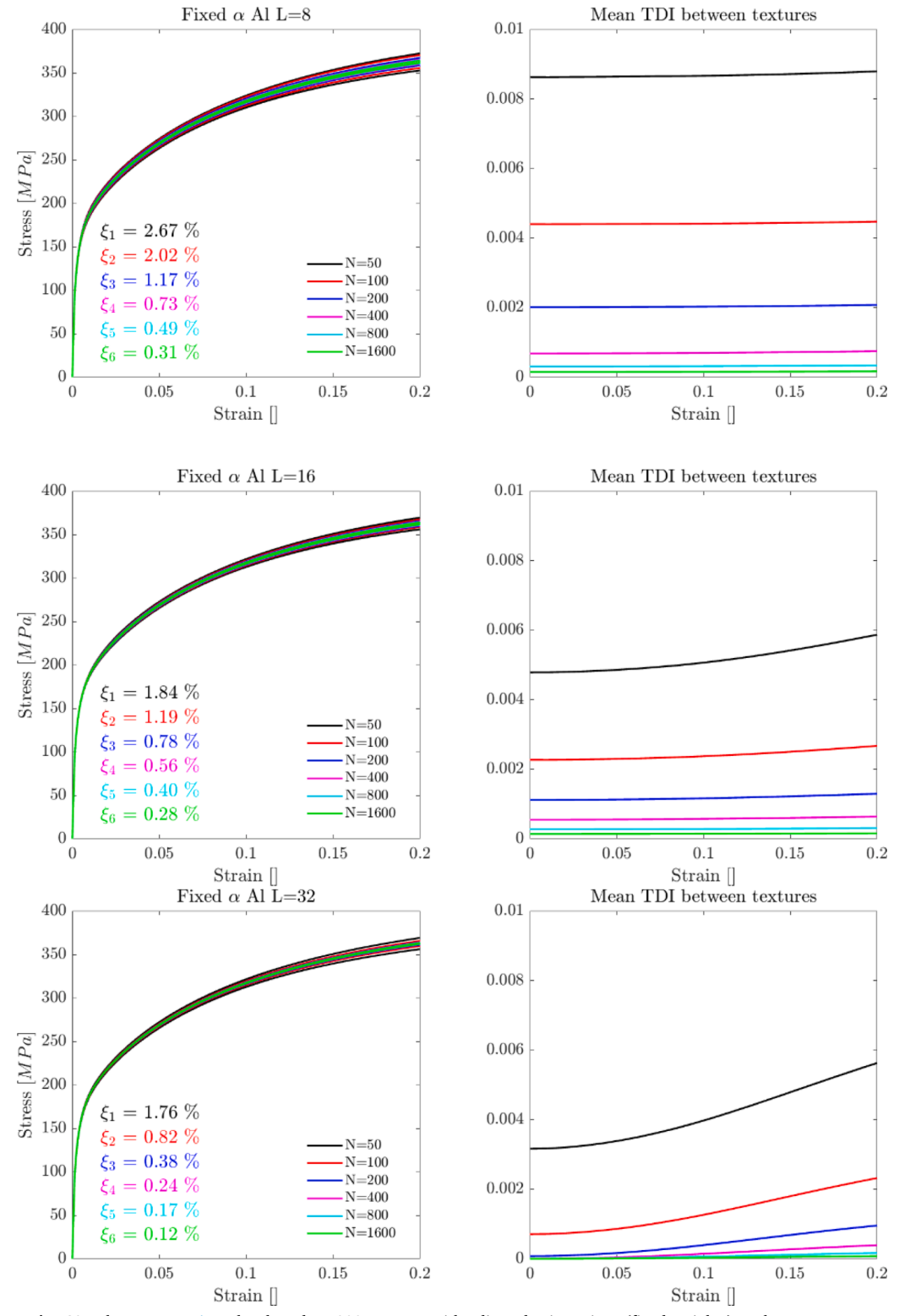


Fig. C3. The same as Fig. 7 but based on 200 textures with adjusted orientations (fixed weights) to the same target.

# References

- Al-Harbi, H.F., Knezevic, M., Kalidindi, S.R., 2010. Spectral approaches for the fast computation of yield surfaces and first-order plastic property closures for polycrystalline materials with cubic-triclinic textures. CMC Comput. Mater. Contin. 15, 153–172.
- Ardeljan, M., Beyerlein, I.J., Knezevic, M., 2014. A dislocation density based crystal plasticity finite element model: application to a two-phase polycrystalline HCP/BCC composites. J. Mech. Phys. Solids 66, 16–31.
- Ardeljan, M., Beyerlein, I.J., McWilliams, B.A., Knezevic, M., 2016. Strain rate and temperature sensitive multi-level crystal plasticity model for large plastic deformation behavior: application to AZ31 magnesium alloy. Int. J. Plast. 83, 90–109.
- Ardeljan, M., Knezevic, M., 2018. Explicit modeling of double twinning in AZ31 using crystal plasticity finite elements for predicting the mechanical fields for twin variant selection and fracture analyses. Acta Mater. 157, 339–354.
- Ardeljan, M., Knezevic, M., Nizolek, T., Beyerlein, I.J., Mara, N.A., Pollock, T.M., 2015. A study of microstructure-driven strain localizations in two-phase polycrystalline HCP/BCC composites using a multi-scale model. Int. J. Plast. 74, 35–57.
- Balasubramanian, 1996. Single crystal and polycrystal elasto-viscoplasticity: application to earing in cup drawing of F.C.C. materials. Comput. Mech. 17, 209–225. Barrett, T.J., Knezevic, M., 2019. Deep drawing simulations using the finite element method embedding a multi-level crystal plasticity constitutive law: experimental verification and sensitivity analysis. Comput. Methods Appl. Mech. Eng. 354, 245–270.
- Barrett, T.J., McCabe, R.J., Brown, D.W., Clausen, B., Vogel, S.C., Knezevic, M., 2020. Predicting deformation behavior of α-uranium during tension, compression, load reversal, rolling, and sheet forming using elasto-plastic, multi-level crystal plasticity coupled with finite elements. J. Mech. Phys. Solids 138, 103924.
- Barrett, T.J., Savage, D.J., Ardeljan, M., Knezevic, M., 2018. An automated procedure for geometry creation and finite element mesh generation: application to explicit grain structure models and machining distortion. Comput. Mater. Sci. 141, 269–281.
- Barton, N., Bernier, J., Knap, J., Sunwoo, A., Cerreta, E., Turner, T., 2011. A call to arms for task parallelism in multi-scale materials modeling. Int. J. Numer. Methods Eng. 86, 744–764.
- Barton, N.R., Knap, J., Arsenlis, A., Becker, R., Hornung, R.D., Jefferson, D.R., 2008. Embedded polycrystal plasticity and adaptive sampling. Int. J. Plast. 24, 242–266.
- Baudin, T., Jura, J., Penelle, R., Pospiech, J., 1995. Estimation of the minimum grain number for the orientation distribution function calculation from individual orientation measurements on Fe-3% Si and Ti-4Al-6V alloys. J. Appl. Crystallogr. 28, 582–589.
- Baudin, T., Penelle, R., 1993. Determination of the total texture. MTA 24, 2299–2311.
- Beaudoin, A.J., Dawson, P.R., Mathur, K.K., Kocks, U.F., Korzekwa, D.A., 1994. Application of polycrystal plasticity to sheet forming. Comput. Methods Appl. Mech. Eng. 117, 49–70.
- Beaudoin, A.J., Mathur, K.K., Dawson, P.R., Johnson, G.C., 1993. Three-dimensional deformation process simulation with explicit use of polycrystal plasticity models. Int. J. Plast. 9, 833–860.
- Beyerlein, I.J., Tóth, L.S., 2009. Texture evolution in equal-channel angular extrusion. Prog. Mater. Sci. 54, 427-510.
- Bunge, H.J., 1993. Texture analysis in materials science. Mathematical Methods. Cuvillier Verlag, Göttingen.
- Bunge, H., 1965. Einige bemerkungen zur symmetrie verallgemeinerter kugelfunktionen. Monatsber. Deutsche Akad. Wiss 7, 351–360.
- Chockalingam, K., Tonks, M.R., Hales, J.D., Gaston, D.R., Millett, P.C., Zhang, L., 2013. Crystal plasticity with Jacobian-Free Newton-Krylov. Comput. Mech. 51, 617–627.
- Daroju, S., Kuwabara, T., Sharma, R., Fullwood, D.T., Miles, M.P., Knezevic, M., 2022. Experimental characterization and crystal plasticity modeling for predicting load reversals in AA6016-T4 and AA7021-T79. Int. J. Plast. 153, 103292.
- EDAX, TSL, 2024. Manual for Orientation Imaging Microscopy (OIMTM), Version 7.1.0.
- Eghtesad, A., Barrett, T.J., Knezevic, M., 2018. Compact reconstruction of orientation distributions using generalized spherical harmonics to advance large-scale crystal plasticity modeling: verification using cubic, hexagonal, and orthorhombic polycrystals. Acta Mater. 155, 418–432.
- Eghtesad, A., Germaschewski, K., Knezevic, M., 2022. Coupling of a multi-GPU accelerated elasto-visco-plastic fast Fourier transform constitutive model with the implicit finite element method. Comput. Mater. Sci. 208, 111348.
- Eghtesad, A., Zecevic, M., Lebensohn, R.A., McCabe, R.J., Knezevic, M., 2017. Spectral database constitutive representation within a spectral micromechanical solver for computationally efficient polycrystal plasticity modelling. Comput. Mech. 61, 89–104.
- Fast, T., Knezevic, M., Kalidindi, S.R., 2008. Application of microstructure sensitive design to structural components produced from hexagonal polycrystalline metals. Comput. Mater. Sci. 43, 374–383.
- Feather, W.G., Ghorbanpour, S., Savage, D.J., Ardeljan, M., Jahedi, M., McWilliams, B.A., Gupta, N., Xiang, C., Vogel, S.C., Knezevic, M., 2019. Mechanical response, twinning, and texture evolution of WE43 magnesium-rare earth alloy as a function of strain rate: experiments and multi-level crystal plasticity modeling. Int. J. Plast. 120, 180–204.
- Feather, W.G., Savage, D.J., Knezevic, M., 2021. A crystal plasticity finite element model embedding strain-rate sensitivities inherent to deformation mechanisms: application to alloy AZ31. Int. J. Plast. 143, 103031.
- Feng, Z., Zecevic, M., Knezevic, M., 2021. Stress-assisted  $(\gamma \rightarrow \alpha')$  and strain-induced  $(\gamma \rightarrow \epsilon \rightarrow \alpha')$  phase transformation kinetics laws implemented in a crystal plasticity model for predicting strain path sensitive deformation of austenitic steels. Int. J. Plast. 136, 102807.
- Gelfand, I.M., Minlos, R.A., Sapiro, Z.S., 1963. Representations of the Rotation and Lorentz Groups and their Applications. Pergamon Press, Oxford, London, UK. Groeber, M., Ghosh, S., Uchic, M.D., Dimiduk, D.M., 2008. A framework for automated analysis and simulation of 3D polycrystalline microstructures. Part 2: synthetic structure generation. Acta Mater. 56, 1274–1287.
- Groeber, M.A., Jackson, M.A., 2014. DREAM. 3D: a digital representation environment for the analysis of microstructure in 3D. Integr. Mater. Manuf. Innov. 3, 5. Kalidindi, S.R., Bronkhorst, C.A., Anand, L., 1992. Crystallographic texture evolution in bulk deformation processing of FCC metals. J. Mech. Phys. Solids 40, 537–569
- Kalidindi, S.R., Duvvuru, H.K., Knezevic, M., 2006. Spectral calibration of crystal plasticity models. Acta Mater. 54, 1795–1804.
- Kalidindi, S.R., Houskamp, J.R., Lyons, M., Adams, B.L., 2004. Microstructure sensitive design of an orthotropic plate subjected to tensile load. Int. J. Plast. 20, 1561–1575.
- Knezevic, M., Al-Harbi, H.F., Kalidindi, S.R., 2009. Crystal plasticity simulations using discrete Fourier transforms. Acta Mater. 57, 1777–1784.
- Knezevic, M., Capolungo, L., Tomé, C.N., Lebensohn, R.A., Alexander, D.J., Mihaila, B., McCabe, R.J., 2012. Anisotropic stress-strain response and microstructure evolution of textured α-uranium. Acta Mater 60, 702–715.
- Knezevic, M., Crapps, J., Beyerlein, I.J., Coughlin, D.R., Clarke, K.D., McCabe, R.J., 2016. Anisotropic modeling of structural components using embedded crystal plasticity constructive laws within finite elements. Int. J. Mech. Sci. 105, 227–238.
- Knezevic, M., Drach, B., Ardeljan, M., Beyerlein, I.J., 2014. Three dimensional predictions of grain scale plasticity and grain boundaries using crystal plasticity finite element models. Comput. Methods Appl. Mech. Eng. 277, 239–259.
- Knezevic, M., Kalidindi, S.R., 2007. Fast computation of first-order elastic-plastic closures for polycrystalline cubic-orthorhombic microstructures. Comput. Mater. Sci. 39, 643–648.
- Knezevic, M., Kalidindi, S.R., Fullwood, D., 2008a. Computationally efficient database and spectral interpolation for fully plastic Taylor-type crystal plasticity calculations of face-centered cubic polycrystals. Int. J. Plast. 24, 1264–1276.
- Knezevic, M., Kalidindi, S.R., Mishra, R.K., 2008b. Delineation of first-order closures for plastic properties requiring explicit consideration of strain hardening and crystallographic texture evolution. Int. J. Plast. 24, 327–342.
- Knezevic, M., McCabe, R.J., Lebensohn, R.A., Tomé, C.N., Liu, C., Lovato, M.L., Mihaila, B., 2013. Integration of self-consistent polycrystal plasticity with dislocation density based hardening laws within an implicit finite element framework: application to low-symmetry metals. J. Mech. Phys. Solids 61, 2034–2046.
- Knezevic, M., Savage, D.J., 2014. A high-performance computational framework for fast crystal plasticity simulations. Comput. Mater. Sci. 83, 101-106.
- Kocks, U.F., Tomé, C.N., Wenk, H.R., 1998. Texture and Anisotropy. Cambridge University Press, Cambridge, UK.

- Landry, N., Knezevic, M., 2015. Delineation of first-order elastic property closures for hexagonal metals using fast fourier transforms. Materials 8, 6326–6345. Lebensohn, R.A., Kanjarla, A.K., Eisenlohr, P., 2012. An elasto-viscoplastic formulation based on fast Fourier transforms for the prediction of micromechanical fields in polycrystalline materials. Int. J. Plast. 32–33. 59–69.
- Lebensohn, R.A., Rollett, A.D., Suquet, P., 2011. Fast fourier transform-based modeling for the determination of micromechanical fields in polycrystals. JOM 63, 13–18
- Lebensohn, R.A., Tomé, C.N., 1993. A self-consistent anisotropic approach for the simulation of plastic deformation and texture development of polycrystals: application to zirconium alloys. Acta Metall. Mater. 41, 2611–2624.
- Lebensohn, R.A., Zecevic, M., Knezevic, M., McCabe, R.J., 2016. Average intragranular misorientation trends in polycrystalline materials predicted by a viscoplastic self-consistent approach. Acta Mater. 104, 228–236.
- Lyon, M., Adams, B.L., 2004. Gradient-based non-linear microstructure design. J. Mech. Phys. Solids 52, 2569-2586.

#### MathWorks, 2023. MATLAB: the language of technical computing.

- Mihaila, B., Knezevic, M., Cardenas, A., 2014. Three orders of magnitude improved efficiency with high-performance spectral crystal plasticity on GPU platforms. Int. J. Numer. Methods Eng. 97, 785–798.
- Panchal, J.H., Kalidindi, S.R., McDowell, D.L., 2013. Key computational modeling issues in Integrated Computational Materials Engineering. Comput. Aided Des. 45, 4–25.
- Pospiech, J., Jura, J., Gottstein, G., 1994. Statistical analysis of single grain orientation data generated from model textures. Mater. Sci. Forum 407-412.
- Proust, G., Tomé, C.N., Kaschner, G.C., 2007. Modeling texture, twinning and hardening evolution during deformation of hexagonal materials. Acta Mater. 55, 2137–2148.
- Raabe, D., Roters, F., 2004. Using texture components in crystal plasticity finite element simulations. Int. J. Plast. 20, 339-361.
- Riyad, I.A., Knezevic, M., 2023. Field fluctuations viscoplastic self-consistent crystal plasticity: applications to predicting texture evolution during deformation and recrystallization of cubic polycrystalline metals. Acta Mater. 261, 119395.
- Roe, R.J., 1965. Description of crystallite orientation in polycrystalline materials. III. General solution to pole figure inversion. J. Appl. Phys. 36, 2024–2031.
- Rollett, A.D., 1997. Overview of modeling and simulation of recrystallization. Prog. Mater. Sci. 42, 79–99.
- Savage, D.J., Beyerlein, I.J., Knezevic, M., 2017. Coupled texture and non-Schmid effects on yield surfaces of body-centered cubic polycrystals predicted by a crystal plasticity finite element approach. Int. J. Solids Struct. 109, 22–32.
- Savage, D.J., Chandola, N., Cazacu, O., McWilliams, B.A., Knezevic, M., 2018. Validation of recent analytical dilatational models for porous polycrystals using crystal plasticity finite element models with Schmid and non-Schmid activation laws. Mech. Mater. 126, 148–162.
- Savage, D.J., Feng, Z., Knezevic, M., 2021. Identification of crystal plasticity model parameters by multi-objective optimization integrating microstructural evolution and mechanical data. Comput. Methods Appl. Mech. Eng. 379, 113747.
- Savage, D.J., Knezevic, M., 2015. Computer implementations of iterative and non-iterative crystal plasticity solvers on high performance graphics hardware. Comput. Mech. 56, 677–690.
- Segurado, J., Lebensohn, R.A., Llorca, J., Tomé, C.N., 2012. Multiscale modeling of plasticity based on embedding the viscoplastic self-consistent formulation in implicit finite elements. Int. J. Plast. 28, 124–140.
- Shaffer, J.B., Knezevic, M., Kalidindi, S.R., 2010. Building texture evolution networks for deformation processing of polycrystalline fcc metals using spectral approaches: applications to process design for targeted performance. Int. J. Plast. 26, 1183–1194.
- Sundararaghavan, V., Zabaras, N., 2007. Linear analysis of texture-property relationships using process-based representations of Rodrigues space. Acta Mater. 55, 1573–1587
- Taylor, G.I., 1938. Plastic strain in metals. J. Inst. Met. 62, 307-324.
- Turner, P.A., Tomé, C.N., 1994. A study of residual stresses in Zircaloy-2 with rod texture. Acta Metall. Mater. 42, 4143-4153.
- Wright, S.I., Adams, B.L., 1990. An evaluation of the single orientation method for texture determination in materials of moderate texture strength. Textures Microstruct. 12. 65–76.
- Wu, X., Proust, G., Knezevic, M., Kalidindi, S.R., 2007. Elastic-plastic property closures for hexagonal close-packed polycrystalline metals using first-order bounding theories. Acta Mater. 55, 2729–2737.
- Zecevic, M., Beyerlein, I.J., Knezevic, M., 2017. Coupling elasto-plastic self-consistent crystal plasticity and implicit finite elements: applications to compression, cyclic tension-compression, and bending to large strains. Int. J. Plast. 93, 187–211.
- Zecevic, M., Beyerlein, I.J., McCabe, R.J., McWilliams, B.A., Knezevic, M., 2016a. Transitioning rate sensitivities across multiple length scales: microstructure-property relationships in the Taylor cylinder impact test on zirconium. Int. J. Plast. 84, 138–159.
- Zecevic, M., Knezevic, M., 2015. A dislocation density based elasto-plastic self-consistent model for the prediction of cyclic deformation: application to Al6022-T4. Int. J. Plast. 72, 200–217.
- Zecevic, M., Knezevic, M., 2017. Modeling of sheet metal forming based on implicit embedding of the elasto-plastic self-consistent formulation in shell elements: application to cup drawing of AA6022-T4. JOM 69, 922–929.
- Zecevic, M., Knezevic, M., 2019. An implicit formulation of the elasto-plastic self-consistent polycrystal plasticity model and its implementation in implicit finite elements. Mech. Mater. 136, 103065.
- Zecevic, M., Knezevic, M., Beyerlein, I.J., McCabe, R.J., 2016b. Texture formation in orthorhombic alpha-uranium under simple compression and rolling to high strains. J. Nucl. Mater. 473, 143–156.
- Schalls, J. Nucl. Mater. 473, 143–130.

  Zecevic, M., Korkolis, Y.P., Kuwabara, T., Knezevic, M., 2016c. Dual-phase steel sheets under cyclic tension–compression to large strains: experiments and crystal plasticity modeling. J. Mech. Phys. Solids 96, 65–87.
- Zecevic, M., Lebensohn, R.A., McCabe, R.J., Knezevic, M., 2018. Modeling of intragranular misorientation and grain fragmentation in polycrystalline materials using the viscoplastic self-consistent formulation. Int. J. Plast. 109, 193–211.
- Zecevic, M., Lebensohn, R.A., McCabe, R.J., Knezevic, M., 2019a. Modelling recrystallization textures driven by intragranular fluctuations implemented in the viscoplastic self-consistent formulation. Acta Mater. 164, 530–546.
- Zecevic, M., McCabe, R.J., Knezevic, M., 2015. A new implementation of the spectral crystal plasticity framework in implicit finite elements. Mech. Mater. 84, 114–126.
- Zecevic, M., Upadhyay, M.V., Polatidis, E., Panzner, T., Van Swygenhoven, H., Knezevic, M., 2019b. A crystallographic extension to the Olson-Cohen model for predicting strain path dependence of martensitic transformation. Acta Mater. 166, 386–401.